


ORIGINAL ARTICLE

Open Access



Active Disturbance Rejection Control of Hydraulic Quadruped Robots Rotary Joints for Improved Impact Resistance

Huaizhi Zong^{1,2}, Zhixian Yang^{1,2}, Xiu Yu³, Junhui Zhang^{1,2}, Jikun Ai^{1,2}, Qixin Zhu^{1,2}, Feng Wang^{1,2*} , Qi Su^{1,2*} and Bing Xu^{1,2}

Abstract

Hydraulic actuated quadruped robots have bright application prospects and significant research values in unmanned area investigation, disaster rescue and other scenarios, due to the advantages of high payload and high power to weight ratio. Among these fields, inevitable collision of robots may occur when contact with unknown objects, step on empty objects, or collapse, all of which have an impact on the working hydraulic system. To overcome the unknown external disturbances, this paper proposes an active disturbance rejection control (ADRC) strategy of double vane hydraulic rotary actuators for the hip joints of the quadruped robots. Considering the order of the valve-controlled actuator model, a three-stage tracking differentiator, a four-stage extended state observer, and a state error feedback controller are designed relatively, and the extended state observer is adopted to observe and compensate the uncertainty of external load torque of the system. The effectiveness of the ADRC method is verified in simulation environment and a single joint experimental platform. Moreover, the impact experiments of the limb leg unit are carried out after introducing the proposed ADRC strategy into hip joint, the limb leg unit of quadruped robots presents better impact resistance ability.

Keywords Quadruped robot, Active disturbance rejection control, Extended state observer, Impact resistance, Hydraulic rotary actuator

1 Introduction

Recently, legged robots have been a hot topic for domestic and foreign researchers to carry out scientific research work, such as imitating the galloping cheetahs for higher motion speed [1], versatile climbing on the ferromagnetic surfaces [2], multimodal locomotion ability [3].

Compared to the wheeled or tracked robots, which rely on continuous contact with the ground, legged robots have the ability to traverse unknown and unstructured terrains easily via dynamically adjusting their leg movements and gaits. Along with the urgent demand for heavy payload and high-speed locomotion, many hydraulic driven quadruped robot prototypes have been developed and applied in payload transportation and uN-manned surveying, including BigDog [4] from Boston Dynamics, HyQ [5] series from the Italian Institutes of Technology, Baby elephant [6] from Shanghai Jiao Tong University.

As the most critical motion unit of quadruped robot, limb leg units play an important role in the locomotion ability of the robots [7]. When working in the complex and rugged terrains [8, 9], the foot ends of limb leg units inevitably contact with the objects in the environment,

*Correspondence:

Feng Wang
dieter@zju.edu.cn
Qi Su
suqi@zju.edu.cn

¹ The State Key Laboratory of Fluid Power and Mechatronic Systems, Zhejiang University, Hangzhou 310027, China

² School of Mechanical Engineering, Zhejiang University, Hangzhou 310027, China

³ China Ship Development and Design Centre, Wuhan 201108, China



© The Author(s) 2024. **Open Access** This article is licensed under a Creative Commons Attribution 4.0 International License, which permits use, sharing, adaptation, distribution and reproduction in any medium or format, as long as you give appropriate credit to the original author(s) and the source, provide a link to the Creative Commons licence, and indicate if changes were made. The images or other third party material in this article are included in the article's Creative Commons licence, unless indicated otherwise in a credit line to the material. If material is not included in the article's Creative Commons licence and your intended use is not permitted by statutory regulation or exceeds the permitted use, you will need to obtain permission directly from the copyright holder. To view a copy of this licence, visit <http://creativecommons.org/licenses/by/4.0/>.

and the expectant control of joint actuators would be affected by the external force transferred from the foot end. In addition, the collision between the foot end and the ground occurs sometimes [10] due to the discontinuous support characteristic although compliance control strategies are employed. If no measures are taken when collision happens, it may affect the position/force tracking performance of the limb leg units, furtherly, resulting in more serious damage to the quadruped robots due to excessive joint output torque. Therefore, it is necessary to estimate and compensate the interference torque in real-time. Furthermore, the joints directly determine the output capacity and the dynamic performance of the legged robots, so optimizing the control method for joints is a key step in improving the impact resistance of the limb leg unit and even quadruped robots.

The control methods of robot joints mainly include adaptive control [11], sliding mode control [12], fuzzy control [13], neural network-based control [14] and other control strategies. Refs. [15–17] designed an adaptive sliding mode controller, which combined the advantages of adaptive backstepping control strategy and sliding mode control strategy to enhance the tracking performance of the whole system. Zhang et al. [18] proposed a multimodal robust adaptive control theory, which involved designing multiple identification models based on the range of parameter uncertainty and adding nonlinear robust terms to the model to suppress the influence of uncertainty and nonlinear factors. Na et al. [19, 20] proposed a control method that need not require backstepping schemes and function approximators, as well as proposing another simple and effective estimation method to handle unknown dynamics and external disturbances in robot system motion control. However, the aforementioned control strategies are often burdened with complicated control laws that proved difficult to fine-tune. On the other hand, the computational complexity associated with these approaches can hinder their applicability in industrial settings. To address these concerns, Han [21, 22] proposed the ADRC algorithm based on in-depth analysis of PID and presented that ADRC was capable of replacing PID strategy with obvious advantage in performance and providing solutions for external disturbances.

The core concept of ADRC strategy revolves around the assimilation of both internal and external uncertainties into a unified disturbance, which is then actively eliminated. This approach stands as a model-free strategy, sparing it from the need for precise knowledge of an accurate parameters and dynamics. To assess the total disturbance, ADRC employs

an extended state observer (ESO), the gain selection of which would largely determine the performance of the ADRC [23–25]. ADRC has been effectively applied to hydraulic quadruped robots. Fan et al. [26] utilized ADRC to improve the control performance and stability of the hydraulic quadruped robot and presented that ADRC controller can keep the robustness, security, and invariability under the indeterminacy dynamic environment, which can greatly meet the requirement of the hydraulic control system. Guo et al. [27] used ADRC in valve-controlled cylinder servo system and demonstrated that ADRC can effectively suppressed the internal parameter changes and external parameter changes of the hydraulic system, and had potential in electrohydraulic systems for high-performance control. Notably, most cases concentrate on position control under unknown disturbances, and the force/torque control of actuators with ADRC has not been reported, especially the hydraulic rotary actuator. Besides, the applications of ADRC in hydraulic quadruped robots require more experimental verification, not just the simulations.

In this paper, a three-stage active disturbance rejection controller is designed to the torque control of a valve-controlled hydraulic rotary actuator, which is to drive the hip joint of the quadruped robots. The input signal is transited via the differential tracker, and a four-stage ESO is expanded to observe the changes of disturbances. Finally, the state error feedback control law is adopted to compensate the error. Simulations are carried out to prove the proposed ADRC strategy is stable and correct. Experiments with the hydraulic actuator are conducted and their results show that the ADRC method has superior performance than that of general PID strategy in overcoming the complicate disturbances. Further experiments are performed in the limb leg unit to show that ADRC can significantly reduce the load torque when the collision occurs.

The main contribution of this paper is to develop a three-stage active disturbance rejection control strategy for a valve-controlled hydraulic rotary actuator and apply it to the hip joint of a hydraulic quadruped robot. This paper is constructed as follows. Section 2 gives the modeling process of the valve-controlled double vane hydraulic rotary actuator. Section 3 describes the design implementations of ADRC controller consisting of three-stage tracking differentiator, four-stage extended state observer, and state error feedback control law. Simulations in the stationary and moving states for hydraulic rotary actuator are shown in Section 4. Then, the experimental results in the level of both hip joint and limb leg unit are expressed in Section 5, followed by the conclusion in Section 6.

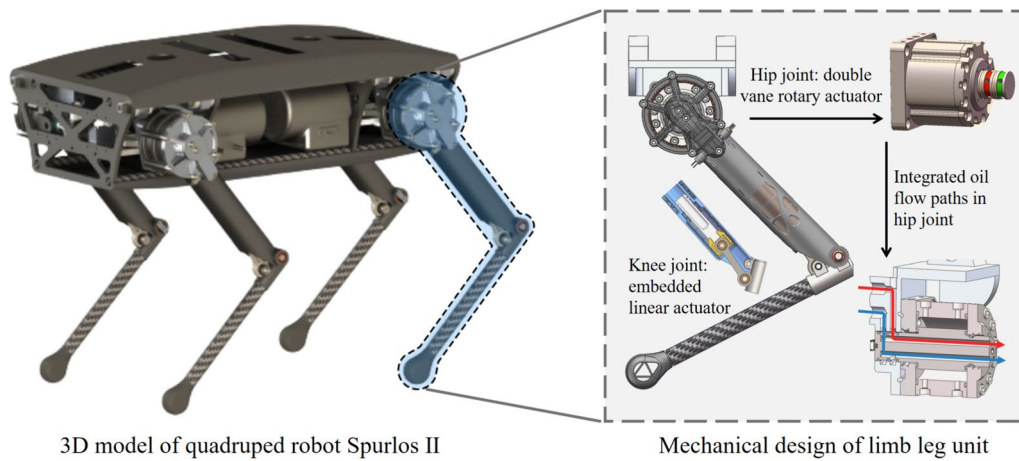


Figure 1 Hydraulic quadruped robot Spurlos II and its hip joint hydraulic rotary actuator

2 Mathematical Model of Valve-controlled Hydraulic Rotary Actuator

2.1 System Overview

Spurlos II, a hydraulic actuated quadruped robot shown in Figure 1, is designed to help humans perform highly challenging tasks such as disaster relief, battlefield reconnaissance, material transportation, and environmental detection on rugged terrain. As the most critical motion unit of quadruped robot, the two-degree-of-freedom limb leg unit depicted in Figure 1, consists of hip and knee joints. The hip joint is driven directly by the double vane rotary actuator, the weight of which is 4.3 kg. The knee joint is actuated by the embedded linear actuator, and the rotational motion is transferred through a centric slider-crank mechanism. The joints are driven by electrohydraulic servo system, consisting of two servo valves, four pressure sensors, two angle encoders, and so on. The limb leg unit weights about 7.8 kg while the shank segment weights about 2.3 kg.

2.2 Mathematical Model

The double vane rotary actuator in hip joint is a key component for the anti-interference control of limb leg unit, whose performance determines the buffering ability of the limb leg unit to various terrains. This paper concentrates on the torque control of the hip joint to realize better impact resistance ability of Spurlos II.

The composition of the valve controlled double-vane rotary cylinder system is shown in Figure 2. The servo valve is the control component, and the swing cylinder is the execution component. According to the oil compressibility and flow continuity, and ignoring internal external leakage [28], the linearization equation of the servo valve flow rate can be written as:

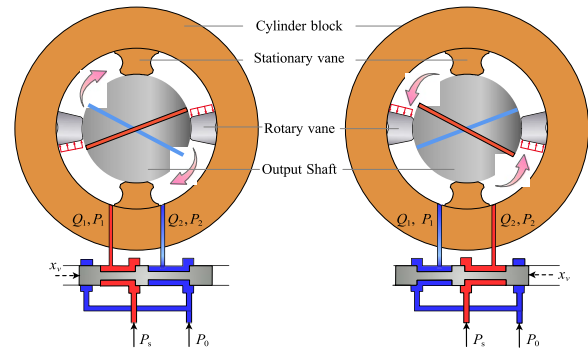


Figure 2 Principle of valve-controlled double vane hydraulic rotary actuator for the hip joint

$$Q_L = K_q X_V - K_c P_L, \tag{1}$$

where K_q is the flow gain of the servo valve, K_c is the amplification coefficient of the flow and pressure of the servo valve, X_V is the displacement of the servo valve spool, and P_L is the load pressure.

Due to the fact that the frequency bandwidth of the servo valve spool is much greater than that of the double vane hydraulic rotary actuator, the servo valve is simplified as a proportional link and expressed by the transfer function:

$$G_{sv}(s) = \frac{X_V}{I_{sv}} = K_v K_{sv}, \tag{2}$$

where I_{sv} is the input current of the servo valve, K_{sv} is the no-load flow gain of the servo valve, and K_v is the controller gain.

The torque sensor and servo amplifier are represented by the following formula:

$$I = K_f \times T, \tag{3}$$

$$I_{sv} = K_a \times I, \tag{4}$$

where K_f is the conversion coefficient of the torque sensor, T is the torque value feedback, I is the output current of the torque sensor, and K_a is the amplifier gain.

The continuity equation for the flow rate of the double-vane rotary cylinder is as follows:

$$Q_L = D_m s \theta + C_{tm} P_L + \frac{V_m}{4\beta_e} s P_L, \tag{5}$$

where D_m is the theoretical displacement of the double-vane rotary cylinder, θ is the output angle, C_{tm} is the leakage coefficient, V_m is the total volume including the connecting oil pipe, and β_e is the elastic modulus of the effective volume.

The load torque balance equation is as follows:

$$T = P_L D_m = J_l s^2 \theta + B_m s \theta + G_m \theta + T_l, \tag{6}$$

where J_l is the moment of inertia of the load torque, B_m is the viscous damping coefficient, G_m is the torsional stiffness of the connecting shaft, and T_l is unknown external interference.

The output torque expression of the valve-controlled double vane hydraulic rotary actuator system can be obtained from Eqs. (1–6) and is shown as:

$$T(s) = \frac{Q(s)(M(s)X_v(s) - N(s)T_l(s))}{As^3 + Bs^2 + Cs + D} + T_l(s), \tag{7}$$

$$\begin{cases} Q(s) = J_l s^2 + B_m s + G_m, \\ M(s) = \frac{K_a}{D_m}, \\ N(s) = \frac{K_{ce}}{D_m^2} \left(\frac{V_m}{4\beta_e K_{ce}} s + 1 \right), \\ A = \frac{J_l V_m}{4\beta_e D_m^2}, \\ B = \frac{J_l K_{ce}}{D_m^2} + \frac{V_m B_m}{4\beta_e D_m^2}, \\ C = \frac{B_m K_{ce}}{D_m^2} + \frac{G_m V_m}{4\beta_e D_m^2} + 1, \\ D = \frac{G_m K_{ce}}{D_m^2}, \end{cases}$$

where $K_{ce} = K_c + C_{tm}$.

Consider $x_1(t)$ as the output torque of the double-vane rotary cylinder, $x_2(t)$ as the rate of change of $x_1(t)$, and $x_3(t)$ as the derivative of $x_2(t)$. According to Eq. (7), a three-stage dynamic system can be obtained as shown in Eq. (8), and the control block diagram of the valve-controlled hydraulic rotary actuator is shown in Figure 3.

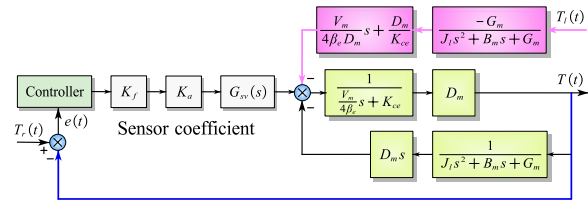


Figure 3 Control block diagram of the valve-controlled hydraulic rotary actuator

$$\begin{cases} \dot{x}_1(t) = x_2(t), \\ \dot{x}_2(t) = x_3(t), \\ \dot{x}_3(t) = a_0 x_1(t) + a_1 x_2(t) + a_2 x_3(t) + bu(t) + d(t), \\ y(t) = x_1(t), \end{cases} \tag{8}$$

where a_0, a_1, a_2, b is the system parameter, which determined via parameters tuning analysis. $y(t)$ is the system output, and $d(t)$ is the interference term.

3 Active Disturbance Rejection Control Strategy Design

For the ADRC strategy, the significance of the controller order cannot be overstated. An improper order selection of controller can directly influence the handling of internal disturbances within the overarching control framework, resulting in the burden on the state observer. Based on the mathematical model of the valve-controlled rotary actuator established in Section 2, traditional two-stage ADRC method needs to be further upgraded, and a three-stage form of ADRC needs to be designed.

As shown in Figure 4, the three-stage ADRC comprises three main sections. The tracking differentiator (Part A) processes the reference input signal, providing smoother and more accurate derivatives of the input. The Extended State Observer (ESO) (Part B) is designed to estimate the system's state variables and the total disturbance, which includes both internal dynamics and external disturbances acting on the system. Finally, the linear state error feedback (Part C) generates the control input that drives the system towards the desired state, based on the estimated states and disturbances from the ESO.

3.1 Design of Three-Stage Tracking Differentiator

The function of tracking differentiator is to arrange the transition process, reduce the jump of input signal, give a reasonable control signal, and solve the contradiction between response speed and overshoot. Considering the order of the controlled object is three, and accordingly, a

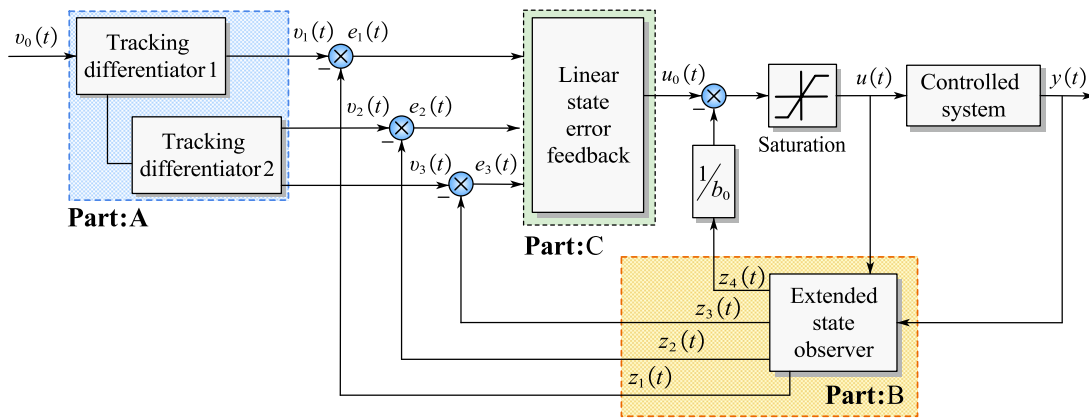


Figure 4 Framework of the proposed ADRC controller

third order tracking differentiator needs to be designed by connecting two tracking differentiators in series shown in Figure 5.

The tracking differentiator unit is designed as:

$$\begin{cases} fh = fhan(v_1(t) - v_0(t), v_2(t), r, h_0), \\ v_1(t) = v_1(t) + hv_2(t), \\ v_2(t) = v_2(t) + hfh, \end{cases} \quad (9)$$

where h is the simulation step size, which is related to the sampling frequency of the system. $v_0(t)$ is the system input, $v_1(t)$ and $v_2(t)$ are the system output derived from tracking differentiator. h_0 is the filtering factor, which can be equal to or slightly greater than h and reduce the random noise interference. r is the speed factor, which determines the speed of tracking the expected torque signal.

fh is a control synthesis function and is implemented as:

$$\begin{cases} d = rh_0, \\ d_0 = h_0d, \\ y = v_1(t) - v_0(t) + h_0v_2(t), \\ a_0 = \sqrt{d^2 + 8r|y|}, \\ a = \begin{cases} v_2(t) + \frac{(a_0 + d)}{2}\text{sign}(y), & |y| > d_0, \\ v_2(t) + \frac{y}{h_0}, & |y| \leq d_0, \end{cases} \\ fhan = -\begin{cases} r\text{sign}(a), & |a| > d, \\ r\frac{a}{d}, & |a| \leq d. \end{cases} \end{cases} \quad (10)$$

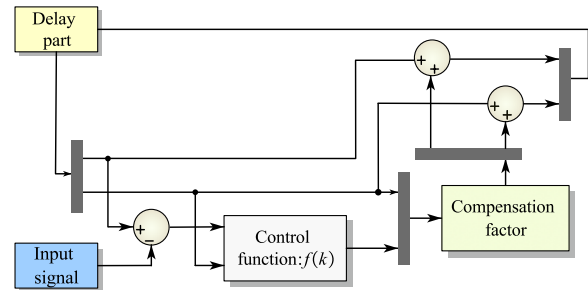


Figure 5 Schematic diagram of tracking differentiator unit

3.2 Design of Four-Stage Extended State Observer

The ESO is adopted to observe the expanded state variables, estimate the unknown disturbance and the unmodeled part of the control object, realizing the feedback linearization of the dynamic system.

The extended state observer of the system is established by tracking and estimating the system state and interference through the input and output of the system:

$$\dot{x}_3(t) = a_0x_1(t) + a_1x_2(t) + a_2x_3(t) + bu(t) + d(t), \quad (11)$$

where a_0, a_1, a_2, b are the system parameters, $y(t)$ are the system output, $d(t)$ is the torque interference term.

Eq. (11) can be rewritten as

$$\dot{x}_3(t) = f(x_1(t), x_2(t), x_3(t), d(t)) + bu(t). \quad (12)$$

The real-time effect of $f(x_1(t), x_2(t), x_3(t), d(t))$ on the system is extended to a new state x_4 , which is expressed as $\dot{x}_4(t) = w(t)$, and the third-stage nonlinear system is further arranged as

$$\begin{cases} \dot{x}_1(t) = x_2(t), \\ \dot{x}_2(t) = x_3(t), \\ \dot{x}_3(t) = x_4(t) + bu(t), \\ \dot{x}_4(t) = w(t), \\ y(t) = x_1(t). \end{cases} \quad (13)$$

Finally, the linear state observer of the extended system is established as follows and shown in Figure 6:

$$\begin{cases} e(k) = z_1(k) - y(k), \\ z_1(k+1) = z_1(k) + h(z_2(k) - \beta_{01}e(k)), \\ z_2(k+1) = z_2(k) + h(z_3(k) - \beta_{02}e(k)), \\ z_3(k+1) = z_3(k) + h(z_4(k) - \beta_{03}e(k) + b_0u(k)), \\ z_4(k+1) = z_4(k) + h(z_2(-\beta_{04}e(k))), \end{cases} \quad (14)$$

where e is the torque output error, z_1 is the estimated value of y , z_2 is the estimated value of the derivative of y , z_3 is the estimated value of the second derivative of y , z_4 is the estimated value of the nonlinear term and external disturbance of the model $\beta_1, \beta_2, \beta_3, \beta_4$ and b_0 are gains.

3.3 Design of State Error Feedback Control Law

The error feedback controller provides the control strategy for the controlled object and compensates for system disturbances through state error feedback. In this system, the design of the state error feedback controller is as follows:

$$\begin{cases} e_1(t) = x_1(t) - z_1(t), \\ e_2(t) = x_2(t) - z_2(t), \\ e_3(t) = x_3(t) - z_3(t), \\ u_0(t) = \alpha_{11}e_1(t) + \alpha_{12}e_2(t) + \alpha_{13}e_3(t), \end{cases} \quad (15)$$

where x_i ($i=1, 2, 3$) is the output value of the tracking differentiator, z_i ($i=1, 2, 3$) is the output value of the extended state observer, α_{1i} ($i=1, 2, 3$) is the gain coefficient of the controller, and u_0 is the control quantity of the error feedback. Considering the external interference of the system, the final output obtained by the linear ADRC controller through compensation is:

$$u(t) = u_0(t) - \frac{z_4(t)}{b_0}. \quad (16)$$

4 Simulation Studies

To verify the effectiveness of the ADRC strategy, a simulation model is built through the SIMULINK module of MATLAB, and the parameter settings are shown in

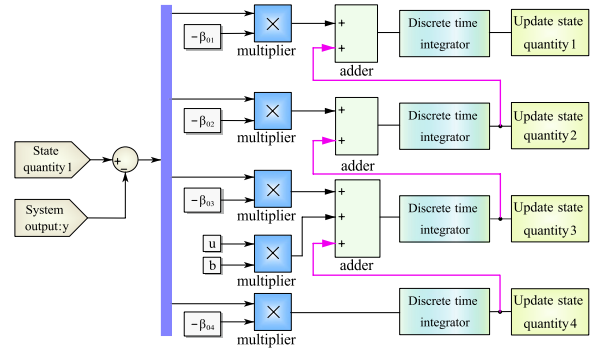


Figure 6 Schematic diagram of the four-stage extended state observer

Table 1. Three working conditions are defined based on the steady states and impact torque value, and the maximum error of output torque after interference, the average error of output torque after interference, and the time to recover stability after interference are adopted as the quantitative performance indicators. Another three working conditions in dynamic state are carried out, and the maximum error and average error of output torque serve as the quantitative performance indicators. The anti-interference effects of ADRC controller and PID controller under different working conditions are compared, further demonstrating the anti-interference ability and adaptability of ADRC controller.

The simulation results under steady state were depicted in Figure 7. In Condition 1, a 65.0 N·m impact torque was applied to the valve-controlled double-vane rotary actuator system. After been disturbed, the maximum error of the actuator output torque with ADRC controller was 18.1 N·m, much less than 60.8 N·m with PID controller. The average errors of the PID controller during the disturbance period was 17.8 N·m, almost three times than that of the ADRC controller. The maximum adjustment time of the ADRC controller was 0.14 s, while the PID controller was 0.21 s. Compared to PID controller, the maximum error of ADRC controller was reduced by 70.2%, the average error was reduced by 69.1%, and the maximum adjustment time was reduced by 33.3%.

When the interference torque increased to 160.0 N·m in Condition 2, the maximum errors of the system output torque under the control of PID and ADRC controllers were 156.4 N·m and 51.8 N·m, with an average error of 25.1 N·m and 12.0 N·m. In addition, the maximum adjustment times were 0.23 s and 0.18 s, respectively. Compared with PID controller, the maximum error, the average error, and the maximum adjustment

Table 1 Parameters for simulation

Parameters	Values
Theoretical discharge capacity D_m (m ³ /rad)	6.12×10^{-5}
System flow pressure coefficient K_{ce} (m ⁵ /Ns)	2.5×10^{-11}
Effective volume V_m (m ³)	5.56×10^{-4}
Effective bulk modulus of elasticity β_e (N/m ²)	6.9×10^8
Equivalent moment of inertia J_l (kg·m ²)	2.23×10^{-3}
Torsional stiffness G_m (N·m/rad)	2.68×10^5
Viscous damping coefficient B_m (N·m·s/rad)	8.0
Servo valve gain K_{sv} (m/A)	1.25×10^{-2}
Torque sensor conversion coefficient K_f (A/N·m)	0.24×10^{-4}
Controller gain K_G (A/V)	3.0×10^{-3}
Servo valve flow gain K_q (m ² /s)	0.98

time of ADRC controller reduced by 66.9%, 52.2%, and 21.7%, respectively.

In Condition 3, the impact torque increased to 310.0 N·m, and better torque performance ability was observed in the ADRC controller. Compared with PID controller, the ADRC controller brought about significant performance improvement: 66.1% reduction in the maximum error of the system output, 45.4% reduction in the average error, 44.4% reduction in the maximum adjustment time.

The simulation results under dynamic state were depicted in Figure 8. In working Condition 4, the actuator was in motion, and a 45.0 N·m interference torque was imposed. The maximum errors of the system output torque under the control of ADRC controller and PID controller were 18.9 N·m and 43.5 N·m, respectively, representing a maximum error reduction of 56.6%. The average errors during the disturbance period were 4.2 N·m and 8.5 N·m, with a reduction of 50.6%. On the basis of Condition 4, Condition 5 and Condition 6 increased the impact torque to 75.0 N·m and 95.0

N·m. In condition 5, Compared with PID controller, the ADRC controller reduced the maximum error by 56.2% and the average error by 54.1%. The maximum error in Condition 6 decreased by 56.3%, and the average error decreased by 57.7%.

In summary, whatever states the valve-controlled double vane hydraulic rotary actuator system were in, the proposed ADRC controller all showed significant improvements in interference resistance.

5 Experimental Studies

To verify the improvement of the anti-interference ability of the controlled object after applying the ADRC controller, experiments were conducted on both the single joint experimental platform and the limb leg unit experimental platform.

5.1 Test Results in the Hip Joint

The framework of the single joint experimental platform system is shown in Figure 9, which consists of a double vane hydraulic rotary cylinder, a servo valve, the CytroPac hydraulic station, a torque sensor, etc. A dynamic torque sensor is used to detect the output torque of the actuator and provide feedback to the ADRC controller to control the opening of the servo valve. The impact experiments were conducted on the single joint experimental platform through sudden loading, and the working conditions were divided by changing the weight of the load and the height of free fall 1.

5.1.1 Steady State Performance

The interference experiments of the double vane rotary cylinder in a stationary state can be divided into three working conditions: Condition 1 (1.0 kg, 0.5 m), Condition 2 (2.5 kg, 0.5 m), Condition 3 (5.0 kg, 0.5 m), shown in Figure 10. In Condition 1, 1.0 kg of load was released at

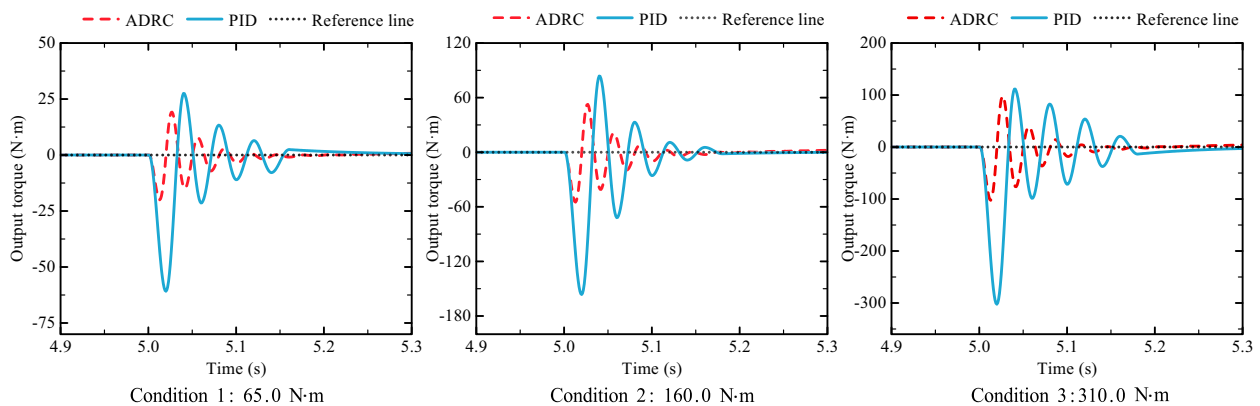


Figure 7 Simulation of actuator output torque curve under steady state

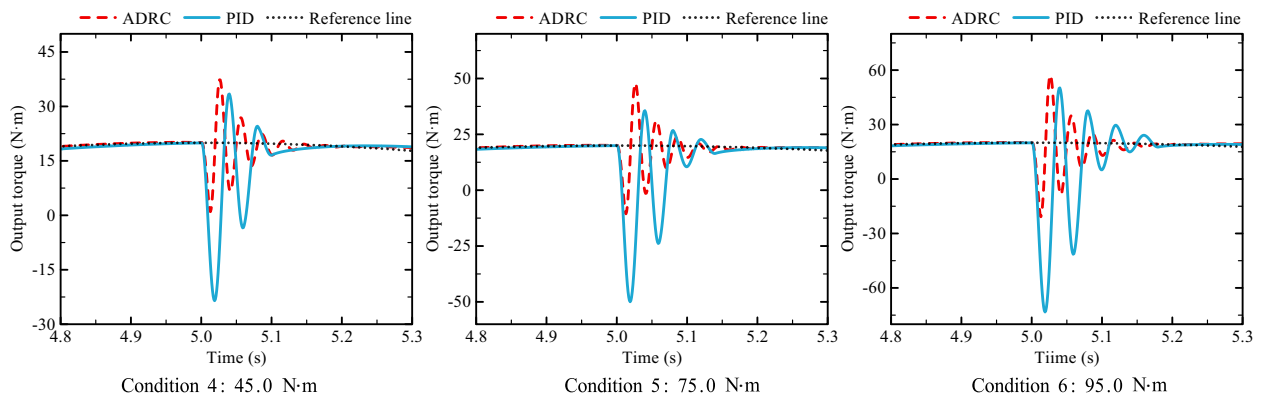


Figure 8 Simulation of actuator output torque curve under dynamic state

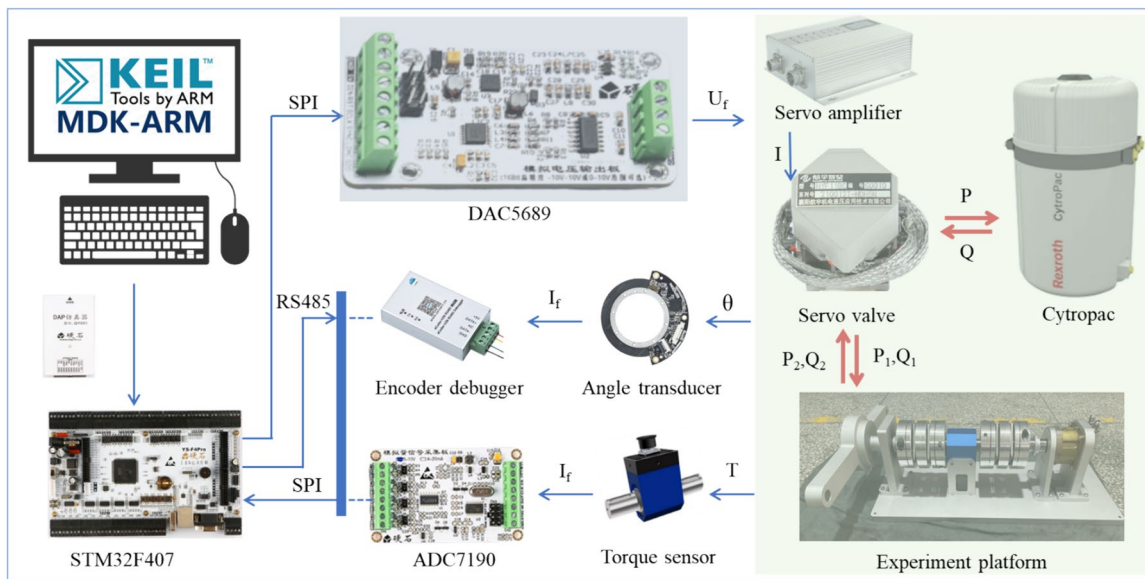


Figure 9 Test platform and schematic diagram of valve-controlled hydraulic actuator system

a height of 0.5 m. According to the experimental curve in Figure 11, the maximum output torque error of the system controlled by the PID controller after interference was 57.4 N·m, and the average error during the disturbance period was 15.9 N·m with a maximum adjustment

time of 0.25 s. The maximum output torque error of the system under the control of ADRC controller after interference was 18.2 N·m, representing a reduction of 68.3%. The average error during the disturbance period was 5.2 N·m, with a maximum adjustment time of 0.19 s.

Table 2 showed the performance comparison in three different conditions. We can see that the ADRC method had a good anti-interference effect, and brought about the maximum torque error reduction of 68.9% in Condition 2 and 69.4% in Condition 3. In addition, the ADRC method contributed to smaller average error, 9.7 N·m in Condition 2 and 23.7 N·m in Condition 3, representing a reduction of 56.1% and 51.65%. Compared with PID method, the proposed ADRC can shorten the adjustment time by 38.1% in Condition 2 and 31.6% in Condition 3.

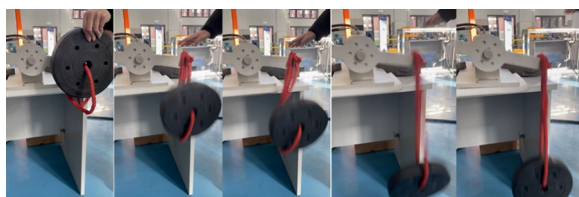


Figure 10 Test rig of imposing the interference torque

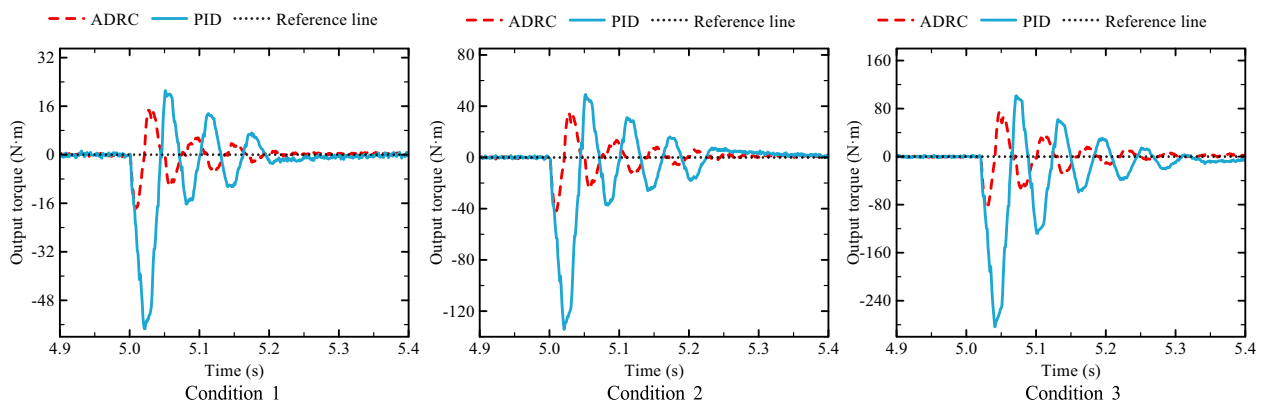


Figure 11 Steady state performance comparisons between PID and ADRC control strategy

5.1.2 Dynamic Performance

When the double vane rotary actuator was in dynamic state that the torque changed from 0–20 N. The interference torque was generated by free fall of an object, and three working conditions were given: Condition 4 (1.0 kg, 0.2 m), Condition 5 (1.0 kg, 0.5 m), Condition 6 (2.0 kg, 0.2 m). The experiment results were depicted in Figure 12. In Condition 4, the maximum output torque in interference direction of the system with ADRC method was $-8.5 \text{ N}\cdot\text{m}$, contrast to $-21.7 \text{ N}\cdot\text{m}$ with PID controller. The maximum output torque error of the PID and ADRC method were $33.4 \text{ N}\cdot\text{m}$, $23.9 \text{ N}\cdot\text{m}$, respectively. The average error during the disturbance period reduced by 16.9% from $8.9 \text{ N}\cdot\text{m}$ to $7.4 \text{ N}\cdot\text{m}$ by changing the PID with ADRC, shown in Table 3.

The same significant performance improvements were observed in Condition 5 and 6. By adopting the ADRC method, the maximum torque in interference direction, the maximum output torque error, and the average error were reduced by 47.7%, 31.3%, and 21.7% (Condition 5); 55.7%, 30.4%, and 21.6% (Condition 6). Consequently, the feasibility of the proposed ADRC strategy was verified from the aspects of maximum output torque in the interference direction, maximum tracking error, and average tracking error.

5.2 Test Results in the Hydraulic Quadruped Robot

After verifying the effectiveness of the ADRC controller at the joint level, it is necessary to verify its effectiveness at the limb leg unit level. An impact experiment based on the limb leg unit is designed in this paper, as shown in Figure 13. The limb leg unit is lifted by the vertical degree of freedom of the limb leg unit experimental platform, and then lifted to a certain height before releasing it at a certain time. The pressure changes in the high and low oil chambers of the joints are measured by installed pressure sensors, and the torque change of the hip joint after the

foot touches the ground is recorded. The hydraulic system pressure was set at 5 MPa, the expected torque is $0 \text{ N}\cdot\text{m}$, and the foot lifting heights are 0.05 m, 0.10 m, 0.15 m, and 0.20 m, respectively.

As shown in Table 4 and Figure 14, when the foot fell 0.05 m off the ground and impacted the hip joint, the difference in the maximum output torque of the system under the control of the two controllers was small, representing $41.5 \text{ N}\cdot\text{m}$ and $36.2 \text{ N}\cdot\text{m}$, respectively. However, the torque fluctuation of the ADRC was relatively minor, and the system restored to the expected torque faster, taking only 0.25 s. Similar results were observed when the foot is 0.10 m off the ground. At a drop height of 0.15 m, the maximum output torque of the hip joint reached $90.0 \text{ N}\cdot\text{m}$ with PID control, whereas it was $55.3 \text{ N}\cdot\text{m}$ with the ADRC controller, reducing by 38.6%. When the dropping height reached to 0.20 m, the ADRC-controlled system exhibited a smaller maximum output torque

Table 2 Performance improvement under steady state

Condition	Performance index	PID	ADRC	Improvement (%)
Condition 1	Maximum tracking error (N·m)	57.4	18.2	68.3
	Average tracking error (N·m)	15.9	5.2	67.3
	Recovery time (s)	0.25	0.19	24.0
Condition 2	Maximum tracking error (N·m)	134.3	41.8	68.9
	Average tracking error (N·m)	22.1	9.7	56.1
	Recovery time (s)	0.42	0.26	38.1
Condition 3	Maximum tracking error (N·m)	283.3	86.7	69.4
	Average tracking error (N·m)	49.0	23.7	51.6
	Recovery time (s)	0.76	0.52	31.6

Table 3 Dynamic performance improvement under dynamic tracking experiments

Condition	Performance index	PID	ADRC	Improvement (%)
Condition 4	Maximum output torque (N·m)	-21.7	-8.5	60.8
	Maximum tracking error (N·m)	33.4	23.9	28.4
	Average tracking error (N·m)	8.9	7.4	16.9
Condition 5	Maximum output torque (N·m)	-38.8	-20.3	47.7
	Maximum tracking error (N·m)	54.9	37.7	31.3
	Average tracking error (N·m)	13.8	10.8	21.7
Condition 6	Maximum output torque (N·m)	-68.0	-30.1	55.7
	Maximum tracking error (N·m)	85.8	59.7	30.4
	Average tracking error (N·m)	21.7	17.0	21.6

than the PID control group, demonstrating a more significant effect in resisting external disturbances. The joint maximum output torque reduced from 113.3 N·m to 84.2 N·m, highlighting the capability of the ADRC controller in observing and compensating for interference. Notably, as the drop height increased, the impact force approached the hip actuator’s maximum output torque, and the adjustable times for both controller were almost the same.

It can be concluded that the maximum torque output of the ADRC control group after being impacted was smaller, which can provide better protection for the hip joint. Moreover, the average torque output before stabilization was diminished, accompanied by a quicker

Table 4 Performance comparison in drop experiments

Falling height	Performance index	PID	ADRC	Improvement (%)
0.05 m	Maximum torque (N·m)	41.5	36.2	12.8
	Average torque (N·m)	22.3	11.0	50.7
	Recovery time (s)	0.34	0.25	26.5
0.10 m	Maximum torque (N·m)	66.5	59.2	11.0
	Average torque (N·m)	18.3	10.6	42.1
	Recovery time (s)	0.57	0.46	19.3
0.15 m	Maximum torque (N·m)	90.0	55.3	38.6
	Average torque (N·m)	17.0	9.3	45.3
	Recovery time (s)	0.63	0.59	6.3
0.20 m	Maximum torque (N·m)	113.3	84.2	68.9
	Average torque (N·m)	17.9	13.8	56.1
	Recovery time (s)	0.69	0.65	5.8

reestablishment of stability post-fluctuation in output torque. These observations collectively substantiate the validity of the proposed ADRC controller in strengthening the hip joint against interferences.

6 Conclusions

This paper focused on the torque control of a valve-controlled double vane hydraulic rotary actuator system, and a three stage ADRC strategy was proposed. The effectiveness of the ADRC method were then verified by simulations, single actuator and limb leg unit experiments. The main conclusions were summarized as follows.

- 1) A mathematical model of the double-vane rotary actuator was established, which determines the order of the ADRC controller. According to the separation

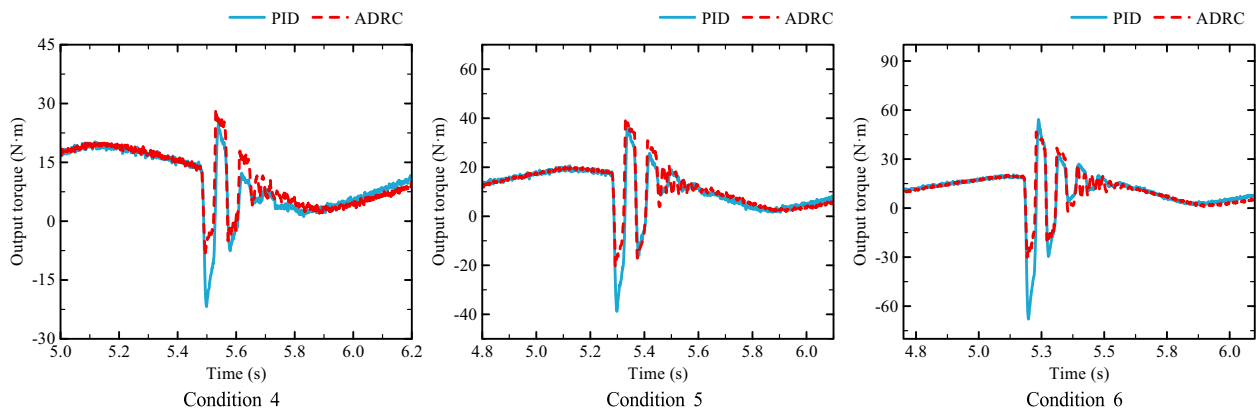


Figure 12 Actuator output torque curve under dynamic state

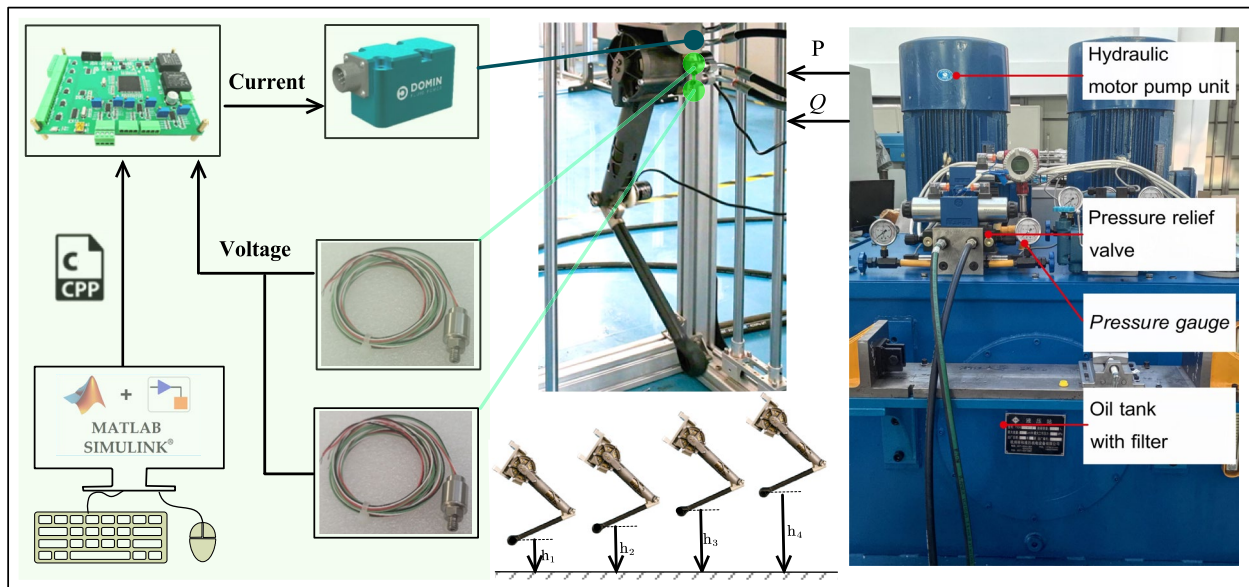


Figure 13 Test rig of the limb leg unit joint impact experiment

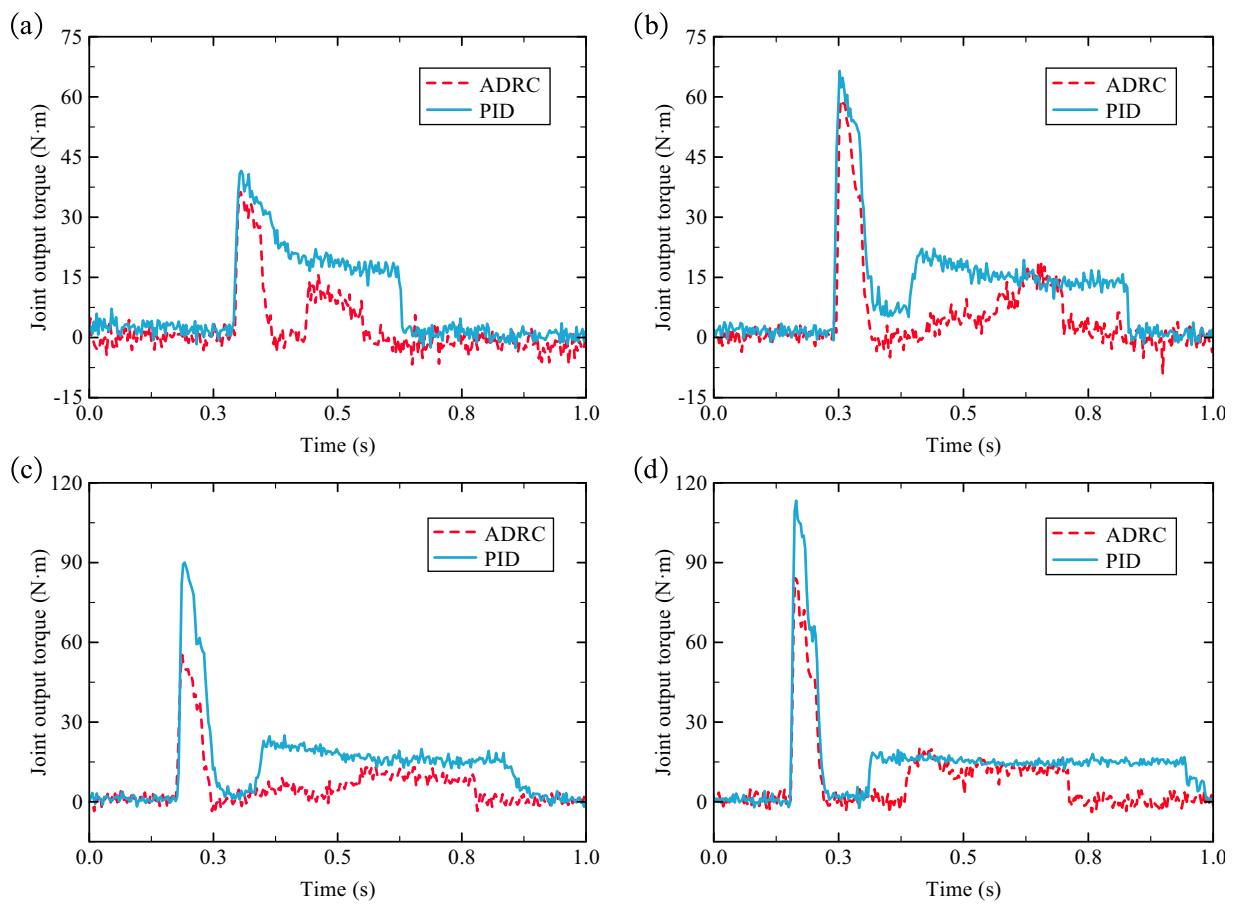


Figure 14 Joint torque change curves under different drop height: (a) 0.05 m, (b) 0.10 m, (c) 0.15 m, (d) 0.20 m

principle for each part, the model of hydraulic rotary actuator and the ADRC controller were built.

- 2) Significant anti-interference ability was observed in both the simulation and the actuator interference test. Moreover, the effectiveness was verified in the steady and dynamic state. Compared with the PID method, the proposed ADRC method presented smaller torque tracking error and shorter recovery time.
- 3) The proposed ADRC controller showed a significant improvement in the anti-interference ability of the system at the joint level and limb leg unit level compared to the PID controller. Furtherly, it can improve the locomotion ability of quadruped robots.

Future work will focus on enhancing the performance of the ADRC method, such as adding leakage compensation for instance, introducing nonlinear control law. Furthermore, realizing the application of ADRC to the quadruped robot Spurlos II is worthy of further research.

Appendix

The detailed proof of four-stage ESO is given. Firstly, according to the stability proof theorem, if **Theorem 1** is satisfied, then the ESO is proven to be stable.

Theorem 1:

(1) For each normal number a , $\lim_{\varepsilon \rightarrow 0} |x_i(t) - z_i(t)| = 0$ is always valid, when $t \in [a, \infty)$;

(2) $\lim_{t \rightarrow \infty} |x_i(t) - z_i(t)| \leq O(\varepsilon^{n+2-i})$

where x_i, z_i are the solutions of Eq. (13) and the ESO, respectively, and $i = 1, 2, \dots, n + 1$, $x_{n+1} = f + w$ represents the expanded state of system (13).

Proof of Theorem 1:

Based on the designed ESO and the defined error, it is known that

$$e_i(t) = x_i(t) - z_i(t). \tag{17}$$

Simultaneously, introducing the scaled estimation error,

$$\eta_i(t) = \frac{\beta_i e_i(\varepsilon t)}{\varepsilon^{n+1-i}}, i = 1, 2, \dots, n + 1. \tag{18}$$

Given that the system is third-order with parameters, and $\eta = [\eta_1, \eta_2, \eta_3, \eta_4]^T$, Then the differential equation for the system is

$$\begin{cases} \dot{\eta}_1(t) = \eta_2(t) - g_1(\eta_1(t)), \eta_1(0) = \frac{\beta_1 e_1(0)}{\varepsilon^4}, \\ \dot{\eta}_2(t) = \eta_3(t) - g_2(\eta_1(t)), \eta_2(0) = \frac{\beta_2 e_2(0)}{\varepsilon^3}, \\ \dot{\eta}_3(t) = \eta_4(t) - g_3(\eta_1(t)), \eta_3(0) = \frac{\beta_3 e_3(0)}{\varepsilon^2}, \\ \dot{\eta}_4(t) = -g_4(\eta_1(t)) + \varepsilon \Delta(t), \eta_4(0) = e_4(0). \end{cases} \tag{19}$$

To prove the convergence of the ESO, the following two assumptions are further made:

Assumption 1: The solutions of system (13) and the ESO are continuously differentiable with respect to their variables, and

$$|w| + |x_i(t)| \leq B, \tag{20}$$

where $B > 0$ and $t \geq 0$.

Assumption 2: There exist constants $\lambda_i (i = 1, 2, 3, 4)$, α, β , a positive definite continuously differentiable function V , and $W: \mathbb{R}^{n+1} \rightarrow \mathbb{R}$, the following equations also hold true:

$$\lambda_1 \|y\|^2 \leq V(y) \leq \lambda_2 \|y\|^2, \lambda_3 \|y\|^2 \leq W(y) \leq \lambda_4 \|y\|^2, \tag{21}$$

$$\sum_{i=1}^n \frac{\partial V}{\partial y_i} (y_{i+1} - g_i(y_1)) - \frac{\partial V}{\partial y_{n+1}} g_{n+1}(y_1) \leq -W(y), \tag{22}$$

$$\left| \frac{\partial V}{\partial y_{n+1}} \right| \leq \beta \|y\|, \tag{23}$$

where $y = (y_1, y_2, \dots, y_{n+1})$, $\|\cdot\|$ denotes the Euclidean norm.

From the above assumptions, it can be inferred that once the designed function is selected and determined, it is necessary to prove the existence of a suitable Lyapunov function V whose derivative along the system satisfies the convergence properties. Since the specific form is not given in this paper, the general form of the Lyapunov function cannot be provided. According to **Assumption 2**, it can be derived that

$$\begin{aligned} \frac{d}{dt} V(\eta(t)) &= \sum_{i=1}^3 \frac{\partial V}{\partial \eta_i} (\eta_{i+1} - g_i(\eta_1)) - \frac{\partial V}{\partial \eta_4} g_4(\eta_1) + \frac{\partial V}{\partial \eta_4} \varepsilon \Delta \\ &\leq -W(\eta) + \varepsilon M \beta |\eta| \leq -\frac{\lambda_3}{\lambda_2} V(\eta) + \frac{\sqrt{\lambda_1}}{\lambda_1} \varepsilon M \beta \sqrt{V(\eta)}. \end{aligned} \tag{24}$$

Based on the relationship between $\sqrt{V(\eta(t))}$ and $V(\eta(t))$, it further follows that

$$\frac{d}{dt} \sqrt{V(\eta(t))} \leq -\frac{\lambda_3}{2\lambda_2} \sqrt{V(\eta(t))} + \frac{\sqrt{\lambda_1} \varepsilon M \beta}{2\lambda_1}. \quad (25)$$

Again, according to **Assumption 2**, it holds that

$$|\eta(t)| \leq \sqrt{\frac{V(\eta(t))}{\lambda_1}} \leq \sqrt{\frac{\lambda_1 V(\eta(0))}{\lambda_1}} e^{-\frac{\lambda_3}{2\lambda_2} t} + \frac{\varepsilon M \beta}{2\lambda_1} \int_0^t e^{-\frac{\lambda_3}{2\lambda_2} (t-s)} ds. \quad (26)$$

Finally, based on the relationship between $\eta(t)$ and $e(t)$, it is obtained that

$$\begin{aligned} |e_i(t)| &= \varepsilon^{4-i} \left| \eta_i \left(\frac{t}{\varepsilon} \right) \right| \leq \varepsilon^{4-i} \eta \left(\frac{t}{\varepsilon} \right) \\ &\leq \varepsilon^{4-i} \left[\sqrt{\frac{\lambda_1 V(\eta(0))}{\lambda_1}} e^{-\frac{\lambda_3 t}{2\lambda_2 \varepsilon}} + \frac{\varepsilon M \beta}{2\lambda_1} \int_0^{\frac{t}{\varepsilon}} e^{-\frac{\lambda_3}{2\lambda_2} (t/\varepsilon-s)} ds \right]. \end{aligned} \quad (27)$$

Given that $\varepsilon = 1$, it is evident that $t \in [a, \infty)$, $|e_i(t)| \rightarrow 0$. The two conclusions of **Theorem 1** can be derived from the above equations. That completes the proof of **Theorem 1**.

Acknowledgements

The authors sincerely thank the Doctoral candidate Kun Zhang, Master candidate Lizhou Fang, for the assistance in processing and experimentation.

Authors' Contributions

Conceptualization: HZZ and JHZ; methodology: HZZ, ZXY, and XY; resources: HZZ, and ZYX; validation: HZZ and ZXY; writing—original draft: HZZ and ZXY; writing—review & editing: HZZ, XY, JKA, and FW; supervision: JHZ, FW, BX, and QS; funding acquisition: QXZ, FW, and BX. All authors have read and agreed to the published version of the manuscript.

Funding

Supported by National Natural Science Foundation of China (Grant No. U21A20124), China Postdoctoral Science Foundation (Grant Nos. 2023T160570, 2022M722737) and the Key Research and Development Program of Zhejiang Province of China (Grant No. 2022C01039).

Data availability

The data are available from the corresponding author on reasonable request.

Declarations

Competing interests

Data available on request from the authors.

Received: 16 August 2023 Revised: 22 June 2024 Accepted: 1 August 2024

Published online: 18 September 2024

References

[1] Y Jin, X Liu, Y Shao, et al. High-speed quadrupedal locomotion by imitation-relaxation reinforcement learning. *Nature Machine Intelligence*, 2022, 4(12): 1198-1208.

[2] S Hong, Y Um, J Park, et al. Agile and versatile climbing on ferromagnetic surfaces with a quadrupedal robot. *Science Robotics*, 2022, 7(73): eadd1017.

[3] K Kim, P Spieler, E S Lupu, et al. A bipedal walking robot that can fly, slackline, and skateboard. *Science Robotics*, 2021, 6(59): eabf8136.

[4] M Raibert, K Blankespoor, G Nelson, et al. Bigdog, the rough-terrain quadruped robot. *IFAC Proceedings Volumes*, 2008, 41(2): 10822-10825.

[5] V Barasuol, O A Villarreal-Magaña, D Sangiah, et al. Highly-integrated hydraulic smart actuators and smart manifolds for high-bandwidth force control. *Frontiers in Robotics and AI*, 2018, 5: 51.

[6] J He, F Gao. Mechanism, actuation, perception, and control of highly dynamic multilegged robots: A review. *Chinese Journal of Mechanical Engineering*, 2020, 33: 79.

[7] Huaizhi Zong, Junhui Zhang, Lei J, et al. Bionic lightweight design of limb leg unit for hydraulic quadruped robots by additive manufacturing and topology optimization. *Bio-Design and Manufacturing*, 2024, 7(1): 1-13.

[8] X Chen, S Zhang, K Cao, et al. Development of a wearable upper limb rehabilitation robot based on reinforced soft pneumatic actuators. *Chinese Journal of Mechanical Engineering*, 2022, 35: 83.

[9] K Xu, P Zi, X Ding. Gait analysis of quadruped robot using the equivalent mechanism concept based on metamorphosis. *Chinese Journal of Mechanical Engineering*, 2019, 32: 8.

[10] J T Kim, J San Cho, B Y Park, et al. Experimental investigation on the design of leg for a hydraulic actuated quadruped robot. *IEEE ISR 2013*, IEEE, 2013: 1-5.

[11] B Xu, J Shen, S Liu, et al. Research and development of electro-hydraulic control valves oriented to industry 4.0: A review. *Chinese Journal of Mechanical Engineering*, 2020, 33: 29.

[12] C Cheng, S Liu, H Wu. Sliding mode observer-based fractional-order proportional-integral-derivative sliding mode control for electro-hydraulic servo systems. *Proceedings of the Institution of Mechanical Engineers, Part C: Journal of Mechanical Engineering Science*, 2020, 234(10): 1887-1898.

[13] X Jin, K Chen, Y Zhao, et al. Simulation of hydraulic transplanting robot control system based on fuzzy PID controller. *Measurement*, 2020, 164: 108023.

[14] J Yao, W Deng. Active disturbance rejection adaptive control of hydraulic servo systems. *IEEE Transactions on Industrial Electronics*, 2017, 64(10): 8023-8032.

[15] Y M Fang, Y C Han, L L Zhao, et al. Adaptive controller for electro-hydraulic servo system with uncertain coefficients in control input. *Control Theory and Applications*, 2009, 26(2): 156-160.

[16] Y M Fang, Z X Jiao, W B Wang, et al. Adaptive backstepping sliding mode control for rolling mill hydraulic servo position system. *Electric Machines and Control*, 2011, 15(10): 95-100.

[17] C Guan, S Pan. Adaptive sliding mode control of electro-hydraulic system with nonlinear unknown parameters. *Control Engineering Practice*, 2008, 16(11): 1275-1284.

[18] Y Zhang, Q Li, W Zhang, et al. Survey of multi-model adaptive control theory and its applications. *Chinese Journal of Engineering*, 2020, 42(2): 135-143.

[19] J Na, Y Li, Y Huang, et al. Output feedback control of uncertain hydraulic servo systems. *IEEE Transactions on Industrial Electronics*, 2019, 67(1): 490-500.

[20] J Na, B Jing, Y Huang, et al. Unknown system dynamics estimator for motion control of nonlinear robotic systems. *IEEE Transactions on Industrial Electronics*, 2019, 67(5): 3850-3859.

[21] J Han. Auto disturbances rejection control technique. *Frontier Science*, 2007, 1(1): 24-31.

[22] J Han. From PID technique to active disturbances rejection control technique. *Control Engineering of China*, 2002, 9(3): 13-18.

[23] X Cheng, X Tu, Y Zhou, et al. Active disturbance rejection control of multi-joint industrial robots based on dynamic feedforward. *Electronics*, 2019, 8(5): 591.

[24] S Chang, Y Wang, Z Zuo. Fixed-time active disturbance rejection control and its application to wheeled mobile robots. *IEEE Transactions on Systems, Man, and Cybernetics: Systems*, 2020, 51(11): 7120-7130.

[25] A J Humaidi, H M Badr, A R Ajil. Design of active disturbance rejection control for single-link flexible joint robot manipulator. *2018 22nd International Conference on System Theory, Control and Computing (ICSTCC)*, IEEE, 2018: 452-457.

- [26] Y Fan, J Shao, G Sun, et al. Active disturbance rejection control design using the optimization algorithm for a hydraulic quadruped robot. *Computational Intelligence and Neuroscience*, 2021: 1-22.
- [27] W Guo, Y Zhao, R Li, et al. Active disturbance rejection control of valve-controlled cylinder servo systems based on MATLAB-AMESim cosimulation. *Complexity*, 2020: 1-10.
- [28] J Shen, J Zhang, H Zong, et al. Hierarchical decoupling controller with cylinder separated model of hydraulic manipulators for contact force/motion control. *IEEE/ASME Transactions on Mechatronics*, 2022, 28(2): 1081-1092.

Huaizhi Zong Received his B.S. degree in 2017 and his M.S. degree in 2020, from *Northeastern University*, and *Zhejiang University, China*, respectively. He is currently pursuing his doctorate at *College of Mechanical Engineering, Zhejiang University*. His research interests include legged robots, lightweight design of hydraulic components, energy recovery and utilization/usage.

Zhixian Yang Received his B.S. degree in 2019 and his M.S. degree in 2023, from *Beijing Institute of Technology*, and *Zhejiang University, China*, respectively. His research interests include joint motion control of hydraulic legged robots.

Xiu Yu Received her B.S. degree in 2017 and her M.S. degree in 2020, from *Donghua University*, and *Zhejiang University, China*, respectively. She is currently working at the Shanghai Branch of *China Ship Development and Design Center*, mainly engaged in ship overall design, unmanned surface vessel, autonomous control system and other related work.

Junhui Zhang Received his B.S. degree in 2007 and his doctorate in 2012, both from *Zhejiang University, China*. He is currently a researcher at *Institute of Mechatronics and Control Engineering, Zhejiang University*. His research interests include high-speed hydraulic pumps/motors, hydraulic robots. He has published more than 100 papers. He is supported by the National Science Fund for Excellent Young Scholars.

Jikun Ai Received his B.S. degree in 2020 and his M.S. degree in 2023, from *Northeastern University*, and *Shanghai Jiao Tong University, China*, respectively. He is currently pursuing his doctorate at *College of Mechanical Engineering, Zhejiang University*. His research interests include hydraulic legged robots and shared control.

Qixin Zhu He is currently a postdoctoral at *Zhejiang University, China*. He received his Ph.D. degree from *Yanshan University, China*, in 2022. His main research interests include design and control of electro-hydraulic servo system, design and control of a hydraulic legged robot.

Feng Wang Received the B.S., M.S., and Ph.D. degrees in mechanical engineering from *Zhejiang University, China*, in 2003, 2005, and 2009, respectively. He is currently a Professor and a Doctoral Supervisor at *Institute of Mechatronic Control Engineering, Zhejiang University*. His research interests include modeling and control of intelligent hydraulic powertrains for heavy-duty vehicles and large utility wind turbines.

Qi Su Born in 1987, is currently an assistant research fellow at *State Key Laboratory of Fluid Power and Mechatronic Systems, Department of Mechanical Engineering, Zhejiang University, China*. He received the B.S. degree in 2010 and the Ph.D. degree in 2016, both from *Zhejiang University, China*. His research interests include electro-hydraulic proportional valve, electro-hydraulic servo control technology, high-speed

on-off valve and system. He published more than 10 papers indexed by SCI, and won 2 first prizes of provincial and ministerial level.

Bing Xu Received his doctorate in fluid power transmission and control from *Zhejiang University, China*, in 2001. He is currently a Professor and a Doctoral Supervisor at *Institute of Mechatronic Control Engineering, Zhejiang University*, and the Deputy Director of the *State Key Laboratory of Fluid Power Transmission and Control, Zhejiang University*. He has authored more than 200 journal and conference papers. Prof. Xu is the Chair Professor of the Yangtze River Scholars Programme, and a science and technology innovation leader of the Ten Thousand Talent Programme.